Energy Reports 7 (2021) 7390–7404

Contents lists available at ScienceDirect

Energy Reports

journal homepage: www.elsevier.com/locate/egyr

Research paper

Techno-economic assessment and optimization of a solar-assisted industrial post-combustion CO_2 capture and utilization plant

Reza Shirmohammadi [a,*], Alireza Aslani [a,*], Roghayeh Ghasempour [a], Luis M. Romeo [b], Fontina Petrakopoulou [c]

[a] Department of Renewable Energies and Environment, Faculty of New Sciences & Technologies, University of Tehran, Tehran, Iran
[b] Escuela de Ingeniería y Arquitectura, Departamento de Ingeniería Mecánica, Universidad de Zaragoza, aría de Luna 3, Zaragoza, 50018, Spain
[c] Department of Thermal and Fluid Engineering, University Carlos III of Madrid, Madrid, Spain

ARTICLE INFO

Article history:
Received 24 August 2021
Received in revised form 4 October 2021
Accepted 18 October 2021
Available online 11 November 2021

Keywords:
Parabolic trough collector
System Advisor Model
Parametric analysis
Solar-assisted carbon capture systems
Industrial process heat

ABSTRACT

This paper studies the techno-economic feasibility of the solar-assisted regeneration process of the largest industrial CO_2 removal monoethanolamine-based plant in Iran. The plant incorporating parabolic troughs is modelled using System Advisor Model software and the weather data are derived from the European Commission's Photovoltaic Geographical Information System. Sensitivity analyses are realized to evaluate the effect of important parameters, i.e., the solar multiple and the hours of storage, and to reveal the optimum case. The studied impacts are linked to the overall net energy generation and the levelized cost of heat (LCOH). The optimum case is found to have a solar multiple of 3.1 and 18-hours of storage, resulting in a solar share of 0.7 and a LCOH of 3.85 (¢/kWh). When compared to the base case (solar multiple of 2 and 6 h of storage), the optimum solution results in a similar LCOH but it achieves the generation of an additional 16,112 MWh_{th} annually. The thermal energy supplied by the solar system leads to an annual reduction in the natural gas consumption of approximately 3.8 million m^3 that results in a CO_2 emission reduction of 7.1 kton.

1. Introduction

CO_2 emissions of power plants and energy intensive industries are the principal causes of climate change (Salkuyeh and Mofarahi, 2012). Undoubtedly, shifting to a low-carbon energy system is required to alleviate global warming. Possible methods to reduce the CO_2 emissions from fossil-fuel-fired plants include: (1) efficiency improvement of the supply and demand, (2) shifting from coal to renewable energies and fuels with high Hydrogen-to-Carbon ratio, and (3) development of carbon capture and utilization plants (Ghoniem, 2011). Furthermore, global climate policies aim to expand the application of renewable energy technologies to battle the adverse effect of CO_2 emissions in regard to climate change. To this end, novel renewable energy-based CO_2 capture systems are being developed and evaluated for practical applications to mitigate environmental emissions (Flores-Granobles and Saeys, 2020; Mokheimer et al., 2020; Siddiqui et al., 2020; Wang et al., 2021a). Although the significance of carbon capture system (CCS) is recognized to fight climate change, its commercial large-scale application is yet to be realized, mainly due to its associated energy penalty (Iribarren et al., 2013; Petrakopoulou and Tsatsaronis, 2014). The thermal energy required to regenerate the solvent in post-combustion CCS is typically provided with low-pressure steam extracted from the plant which leads to some efficiency penalty (Shirmohammadi et al., 2018; Petrakopoulou et al., 2012). For this reason, solar-assisted carbon capture systems (SACCS) have been developed to supply full or part of the thermal energy demand with solar energy (STE) (Wang et al., 2021b).

After wide attention in the 1970s, yet few deployments, the application of concentrating solar technologies for thermal and industrial purposes have been increasing (Schoeneberger et al., 2020). Wibberley (2010) initially developed the amine-based solar-assisted post-combustion carbon capture (SPCC) in which STE was employed to regenerate the solvent. Parabolic trough collector (PTC) and flat plate collectors have been widely considered because of their capability to provide low-grade thermal energy desired for solvent regeneration (SR). To reduce the exergy destruction in a heat transfer process the temperature difference across which the heat exchange taking place must be minimized. This makes the choice of the appropriate solar thermal collectors (STC) very important. Extensive overviews of amine-based SPCC have been conducted. Parvareh et al. (2014) divided SACCSs into full or partial solar-assisted systems on the basis of solar fraction. Saghafifar and Gabra (2020) categorized these systems into

* Corresponding authors.
E-mail addresses: r.shirmohammadi@ut.ac.ir (R. Shirmohammadi), alireza.aslani@ut.ac.ir (A. Aslani).

https://doi.org/10.1016/j.egyr.2021.10.091

indirect solar assisted (ISA) and direct solar assisted (DSA) CCSs depending on the connection between STCs and CCSs. Studies on diverse features of ISA and DSA amine-based SACCS are presented in Table 1.

Khalilpour et al. (2017) utilized STE to heat up the solvent directly. The solvent, used as the heat transfer fluid (HTF), was stored in a two-tank storage unit that intrinsically saved STE. However, it was reported that the technical possibility and operating factors of the combination of STC with the regeneration system without any connecting medium must be further experimentally investigated. Zhai et al. (2017) proposed two configurations with STC integration. Inconsistency between the STC and operating temperatures of the regeneration was found and partly fixed in direct systems. To realize that the high-quality solar energy was initially used to increase the feed water temperature and the low-grade heat was then employed to regenerate the solvent. Li et al. (2012) conducted an analysis to compare the integration of PTC and evacuated tube collector (ETC) within a post-combustion carbon capture (PCC) unit. This study emphasized the significance of STC integration in this application in terms of operating temperature and showed that capital cost of STC increases with the operating temperature. Qadir et al. (2013) examined the effect of five different collectors, i.e., PTC, ETC, compound parabolic collector (CPC), flat plate collector (FPC), and linear Fresnel collector (LFC). Their results showed that optimization of heat integration by means of low temperature STCs is very important. They reported that the accessible low-quality heat at the reboiler outlet could be used for heating a low-temperature process stream. Finally, they improved the overall thermal performance by utilizing useful waste heat. Wang et al. (2015) conducted experiments on an integrated laboratory-scale pilot plant with linear Fresnel collectors and PTC. They concluded that integration of STE for SR causes a vast disruption in the operation of the system because of the variability and intermittency of the solar energy. Wang et al. (2017a) also studied the same setup as an continuance of the earlier work, and discussed the advantages and disadvantages of SACCSs. Their results showed the significance of the consistency and dynamic reply of the system in terms of sporadic operational conditions. Qadir et al. (2015a) investigated various features of SPCC in Australia. They concluded that the system had better to generate additional electricity. Moreover, the LCOE of the SPCC as found to be higher than that of the system not integrated with solar energy. However, these results may vary on the available solar source, the price of the electricity and the CO_2 emissions of a particular region.

In this paper, a techno-economic analysis of an industrial SPCC is carried out using the System Advisor Model (SAM) software. To the best of our knowledge, there is no other work in literature presenting the analysis of an industrial SPCC. This work explores the possibility of integrating a solar industrial process heat (SIPH) to an industrial CO_2 capture and utilization (CCU) unit. The developed structure is a solar-assisted CCU plant coupled with an ammonia plant utilizing from low-pressure steam from an ammonia reformer. The SIPH system is driven by the heat absorbed by the HTF. The heat is transferred to the water through a heat exchanger generating steam and it is then used to regenerate the solvent. Integrated thermal storage provides the required thermal load when solar radiation is not available. Parametric studies are then conducted considering main variables, i.e., the solar multiple (SM) and the hours of storage, in order to optimize the overall net energy and the levelized cost of heat (LCOH). A detailed analysis of the selected case is then realized.

2. Case study

The structure studied here is a solar-assisted CCU plant, receiving low-pressure steam from the ammonia reformer of an ammonia plant. Petrochemicals have been considered as a great potential for implementing and integrating of CCU plants, also because of the possibility to increase the product capacity of the plant by producing of new product (Shirmohammadi et al., 2020a). The operational data for simulation of the CCU plant included in the SPCC plant studied here is provided by Kermanshah Petrochemical Industries Co (KPIC). KPIC is involved in manufacturing and selling agricultural fertilizers and chemicals and produces urea fertilizer, liquid ammonia, and liquid nitrogen (Shirmohammadi et al., 2021). The simulation of the CCU plant is presented in Shirmohammadi et al. (2020b).

Fig. 1 shows the schematic of the SPCC system. The solar field (SF) made of trough-shaped collectors gathers the heat received from the sun onto tubular receivers. Every collector includes mirrors and supporter structures allowing it to track the sun and resist wind-induced forces. The receivers are made of a metal tube with an absorbing surface in a vacuum inside a coated glass tube. Heat is transported by a HTF from the SF to the regenerator. The required thermal energy for the reboiler can be supplied by solar energy or steam from other units such as low-pressure steam of turbines. In this case, most of the required energy for the SR is supplied by STE, while the remaining is provided by steam from the reformer in the ammonia plant. When there is plenty of solar irradiation, the working fluid heats up, part of it is stored in the thermal energy storage (TES), while the remaining part is used to generate steam for the SR. When there is not enough solar energy, stored thermal energy from the TES supplemented by steam extraction from the ammonia reformer are used for the SR. There are noteworthy differences in solar irradiation and ambient temperature in the different seasons. The SF is designed based on monthly climate data of a typical year and the TES is designed to provide energy for a specific predetermined amount of hours.

3. The solar industrial process heat model

The weather data for the case study is based on data for a representative year, as provided by European Commission's Photovoltaic Geographical Information System (PVGIS) (Pvgis, 2018). PVGIS is a free and open-access web site that provides data on solar radiation as well as photovoltaic system performance. The website can also be used to calculate the amount of energy generated from various kinds of solar systems at nearly any place in the world.

The plant is simulated using the chemical process simulator ASPEN Hysys® V. 10, incorporating the Acid Gas Property Package models to calculate the thermodynamic properties (Dubois and Thomas, 2018). The CCU plant consists of three columns, i.e., the soda ash wash-direct contact column and the absorption and stripper columns. The soda ash wash-direct contact column consists of two packed sections with a diameter of 3.8 m and a height of 6 m. The absorber has 5 sections with a height of 13 m. The cooling and washing sections are located at the top part and two intercoolers are placed in the middle section of the column. The lean solvent is delivered to the third segment of the absorber, where the absorption with the aqueous solution MEA takes place. The washing section uses a contact-cooler to avert water equilibrium, as well as amine loss. Two intercoolers situated at a height of 3 and 6 m in the middle section of the absorption column lead to surging in absorption rate. The rich solution is heated and refluxed in the two-stage rich-lean heat exchangers using heat from stream and the regenerated solution.

Table 1
Summary of existing research on SACCS.

References	Year	Location	Capacity	Integration scheme	Solar fraction (%)	Solar thermal collector	Working fluid	Operating temperature (°C)
Li et al. (2012)	2012	China & USA	520 MWe	DSA	Nominal: 30–90	ETC & PTC	Steam	160
Mokhtar et al. (2012)	2012	Australia	300 MWe	DSA	Annual: 0–70	LFC	Steam	140
Zhao et al. (2012)	2012	China	–	DSA/ISA	Annual: 27.6	PTC	Steam	<200/300
Qadir et al. (2013)	2013	Australia	660 MW	DSA	Annual: 0–90	LFC, PTC, ETC, FPC & CPC	Steam	120
Zhao et al. (2014)	2014	China	330 MWe	ISA	–	PTC	Thermal oil	330
Carapellucci et al. (2015a)	2015	Italy	100 MWe	DSA	Maximum: 80	LFC	Steam	133.5
Brodrick et al. (2015)	2015	USA	440 MWe	ISA	–	PTC	Steam	336 °C
Carapellucci et al. (2015b)	2015	Italy	100 MWe	DSA	Maximum: 83	LFC	Steam	270
Qadir et al. (2015b)	2015	Australia	660 MWe	DSA/ISA	–	PTC	Therminol VP-1	120/250
Parvareh et al. (2015)	2015	Australia	660 MWe	ISA	–	PTC	Therminol VP-1	270
Wang et al. (2017a)	2015	–	–	DSA	–	LFC & PTC	Steam	140
Khalilpour et al. (2017)	2017	Australia	660 MWe	DSA	Annual: 83.9	PTC	MEA	120
Wang et al. (2017b)	2017	China	300 MWe	DSA/ISA	Annual: 30.02	PTC	Steam	~200/200–400
Zhai et al. (2017)	2017	China	1000 MWe	DSA/ISA	–	PTC	Steam	387.7

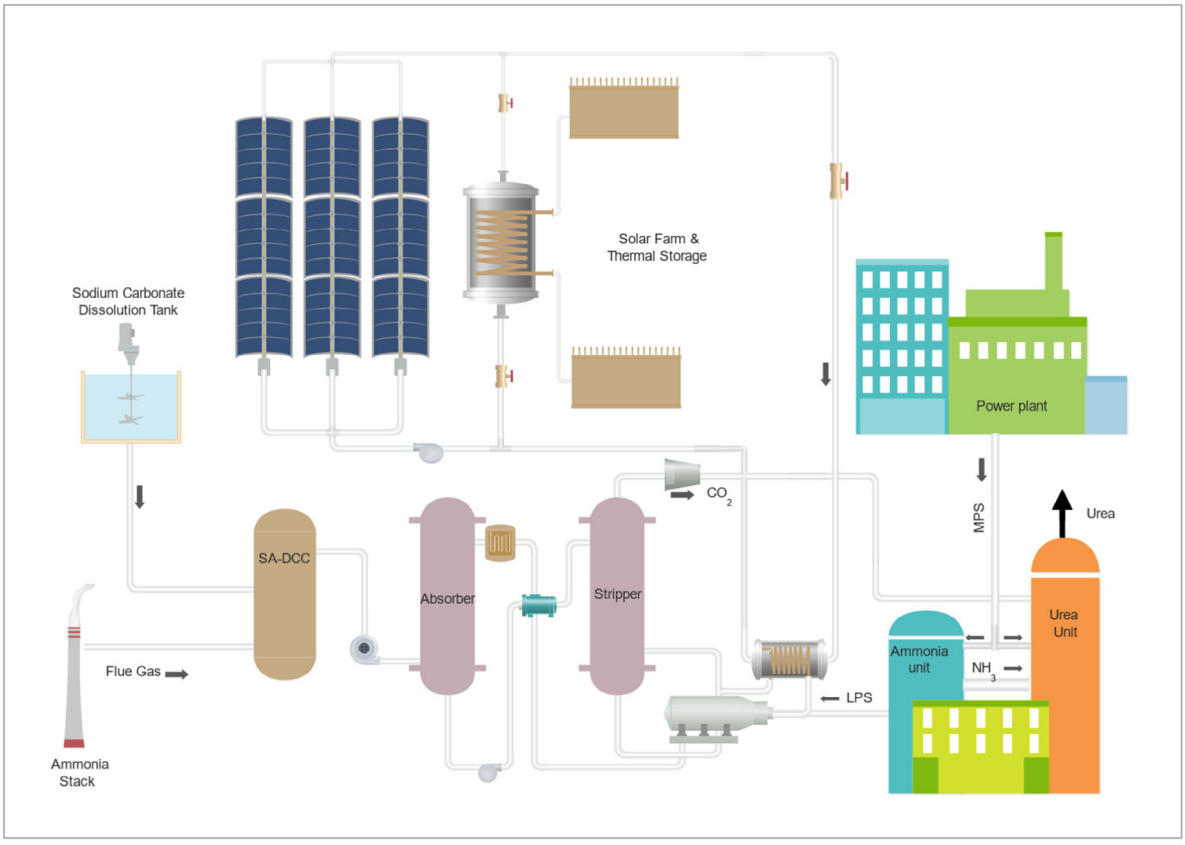

Fig. 1. Schematic of the SPCC system.

Then the rich solvent is delivered to the top segment of the stripper, where the solvent regeneration is completed. The stripper has two packed sections, excluding the cold striper, with the total height of 9 m. The solvent is then delivered to the condenser where the vaporized part is separated and relatively pure CO_2 with a molar concentration of 95% is delivered to the compressor of the Urea plant. A flow diagram of the CCU plant is shown in Fig. 1.

To realize the techno-economic analysis of the system including the industrial process heat from parabolic troughs, the software SAM is used that incorporates the transient system (TRNSYS) simulation tool for modelling (Blair et al., 2014). SAM is a software developed by the National Renewable Energy Laboratory (NREL) able to evaluate diverse renewable energy systems using economic analyses. Here the latest version of SAM software, i.e., 2020.2.29 is used (Lopes et al., 2020). The weather data for the case study are derived from PVGIS and added to the solar resource

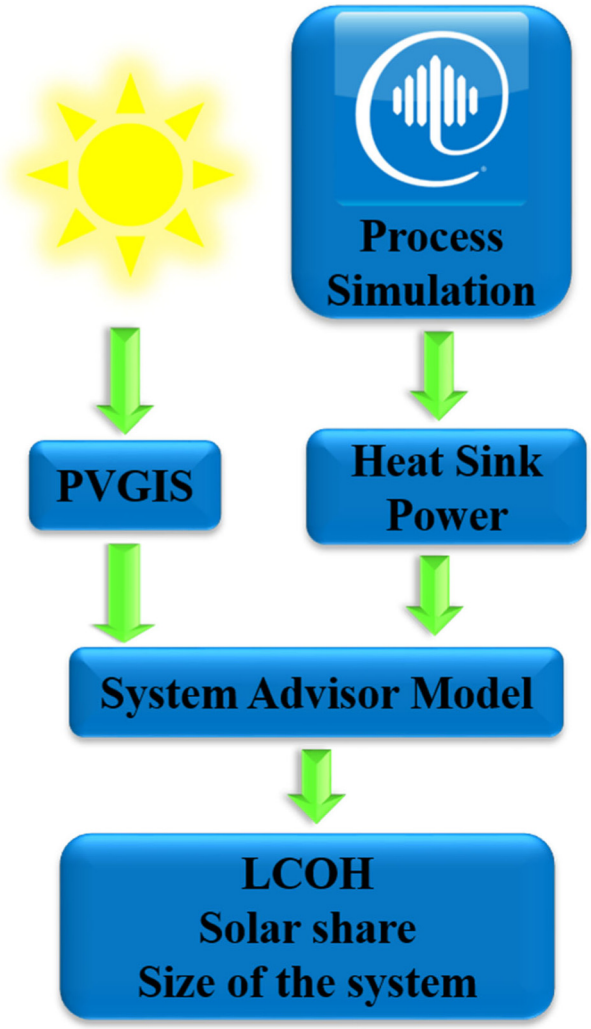

Fig. 2. Interrelation of the software used in the calculation process.

library of SAM. The required energy for the SR is calculated with the ASPEN Hysys software and the value is imported as a heat sink power to the SAM. The heat sink power is the demand of the stripper (constant). Fig. 2 presents the way in which the tools are linked together.

SAM provides a detailed design along with an hourly simulation for the system. Modelling by SAM requires input to define the features of the physical equipment of the system and estimated the costs of the project. The receiver and the collector are initially configured, followed by the specification of the HTF and the operating temperatures that specify the design point of the cycle. Then, parameters related to the thermal storage are configured, to obtain the economic results. Eventually, the optimum case considering of the SM and the TES capacity is received.

4. Site characteristics and key performance indicators

Iran has affluent space and plenty of solar hours. This leads to attracting local and international investment in solar power generation. Bisotun is located in the Kermanshah province in western Iran. The latitude and longitude of the location are 34.356 and 47.431, respectively. Fig. 3 shows the resource beam normal irradiance (W/m^2) for the case study. Fig. 4 shows the variation of the DNI and the dry bulb temperature for a summer day (1 July).

Several key performance indicators are considered for the design of solar plants. The design of the SF is the starting and most significant decision parameter. The heat sink power, defined as thermal input at the design point, is set to 7.44 MWh$_{th}$. The hours of the TES at full load is set to 6 h. The HTF (working fluid) selected is the Hitec XL. The design point DNI is set to 850 W/m^2. The angle between the plane of the collector and the horizon (tilt) is set to the latitude of the location. The azimuth angle is set to 0°. The target SM is the ratio of the target receiver thermal power and heat sink power at the design point, defined as follows:

$$SM = \frac{\text{Receiver thermal power (MWth)}}{\text{Heat sink power (MWth)}} \tag{1}$$

where, the receiver thermal power is the power required at the receiver outlet to meet the design thermal load, and the heat sink power expresses the thermal load of the process heat. The SM can oversize the receiver design output relative to the heat sink and is herein set to 2.

5. The calculation method of the LCOH

To obtain the LCOH for the system, the fixed charge rate (FCR) of the project needs to be calculated. The financial assumptions include a ten-year period, with an inflation rate of 2.5%, a nominal debt interest rate of 5% and an annual effective tax rate of 20%. The FCR represents the required annual income from the project to make up for its investment cost and it is obtained with the following equation:

$$FCR = CRF * PFF * CFF \tag{2}$$

where, CRF stands for capital recovery factor, PFF for project financing factor, and CFF for construction financing factor. SAM calculates the FCR from a set of financial assumptions using the following equations to calculate the CRF, PFF and CFF:

$$CRF = \frac{WACC}{1 - \frac{1}{(1+WACC)^n}} \tag{3}$$

where, WACC stands for the weighted average cost of capital in period N. The WACC is obtained with the equation given in Box I, where, RROE is the real return on investment, RINT is the real-debt interest rate and tax is the rate of effective tax. The RROE is defined as:

$$\text{RROE} = \frac{1 + \text{IRR}}{1 + \text{i}} - 1 \tag{5}$$

where, IRR is nominal return on investment.

RINT is obtained by the following equation:

$$\text{RINT} = \frac{1 + \text{NINT}}{1 + \text{i}} - 1 \tag{6}$$

with NINT the nominal-debt interest rate.

PFF is a function of the depreciation schedule and the rate of effective tax:

$$\text{PFF} = \frac{1 - \text{TAX} \times \text{PVDEP}}{1 - \text{TAX}} \tag{7}$$

where, PVDEP is the present value of depreciation, obtained as:

$$PVDEP = \sum_{n=0}^{N} \frac{DEP_n}{((1 + \text{WACC}) \times (1 + i))^{(n+1)}} \tag{8}$$

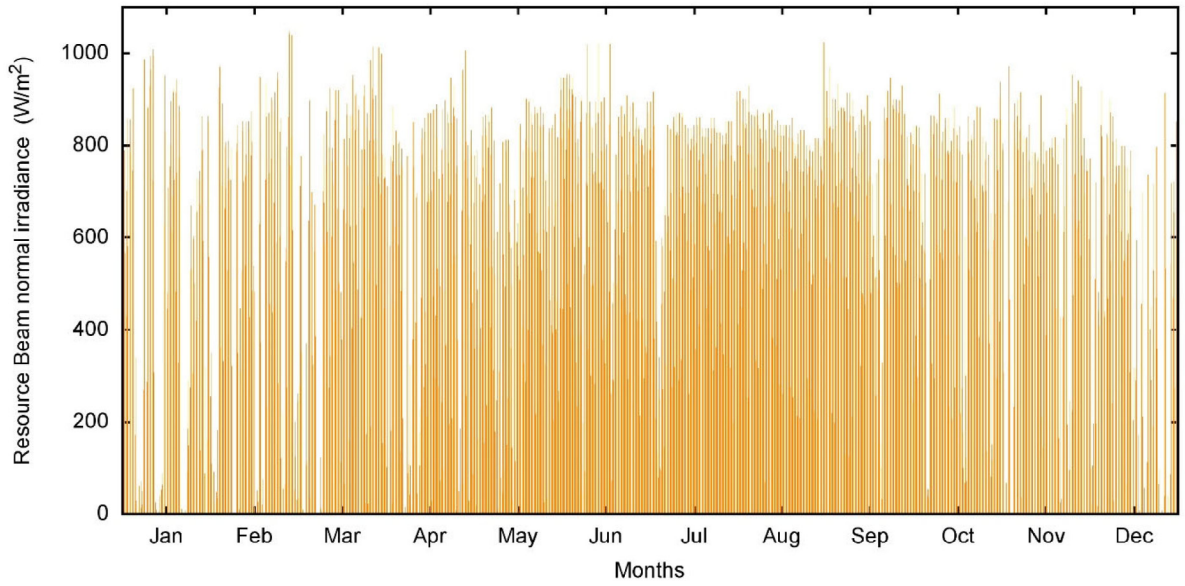

Fig. 3. Resource beam normal irradiance in Bisotun (W/m^2).

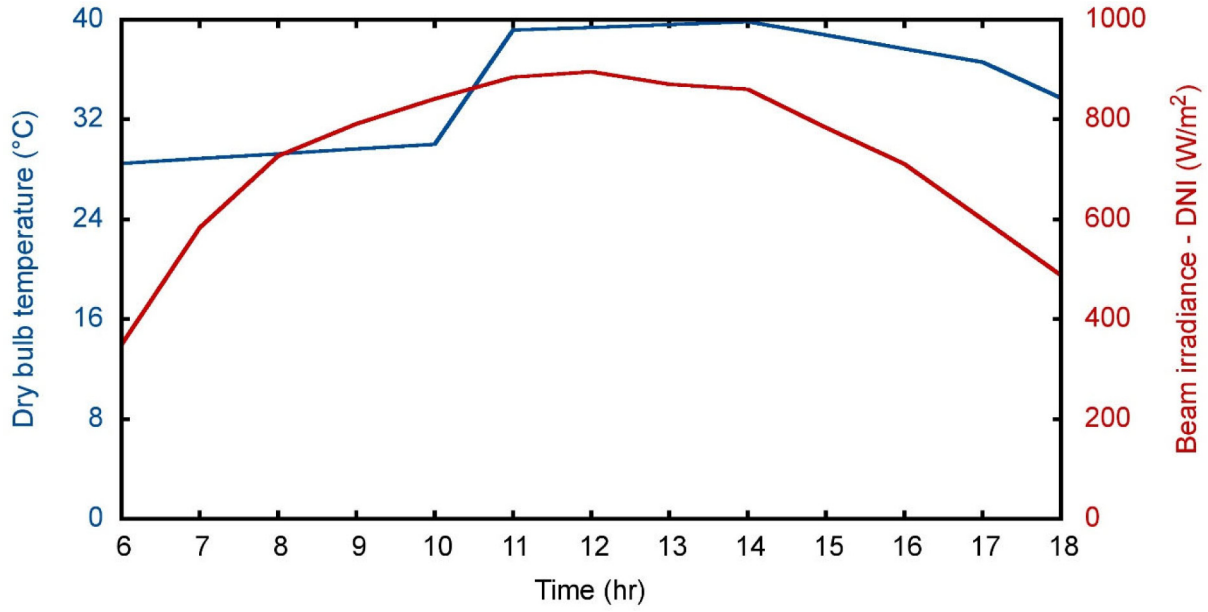

Fig. 4. Variation of the DNI and dry bulb temperature on the 1st of July.

$$\mathrm{WACC} = \frac{1 + ((1 - DF) \times ((1 + RROE) \times (1 + i) - 1)) + DF \times ((1 + RINT) \times (1 + i) - 1) \times (1 - TAX)}{1 + \mathrm{i}} - 1 \quad (4)$$

Box I.

CFF is calculated as:

$$CFF = \sum_{c=0}^{c} CON_c \times \left(1 + (1 - TAX) \times ((1 + CINT))^{(c+0.5)} - 1\right) \quad (9)$$

where, CINT is the nominal construction financing interest rate.

With all above parameters estimated, FCR is calculated using Eq. (2). Thus, the LCOH is:

$$LCOH = \frac{FCR * TCC + FOC}{AEP} + VOC \quad (10)$$

where, TCC is the total capital cost, $; FOC is the fixed annual operating cost, $; VOC is the variable operating cost, $/kWh; AEP is the annual energy production (Ezeanya et al., 2018).

6. Optimization process

In this study, the integrated analytic hierarchy process (AHP) and technique for order preference by similarity to ideal solution (TOPSIS) method is implemented. AHP has been used in the analysis of decision problems related to renewable energy systems (Gutierrez et al., 2021). The pair-wise comparison matrix is created based on the judgements of experts using the fundamental scale of AHP, Eq. (11) (Saaty, 1988).

$$A = \begin{bmatrix} a_{11} & a_{12} & \cdots & a_{1n} \\ a_{21} & a_{22} & \cdots & a_{2n} \\ \cdots & \cdots & \cdots & \cdots \\ a_{n1} & a_{n2} & \cdots & a_{nn} \end{bmatrix} \tag{11}$$

$$a_{ij} > 0. a_{ij} = \frac{1}{a_{ji}}. a_{ii} = 1$$

In this equation a_{ij} is the decision-maker's preference of the ith criterion over the jth criterion. The normalized pair-wise matrix is built by dividing each element of matrix A with the sum of the column the element belongs to (Eq. (12)):

$$X = \begin{bmatrix} \frac{a_{11}}{\sum_{n=1}^{n} a_{n1}} & \frac{a_{12}}{\sum_{n=1}^{n} a_{n2}} & \cdots & \frac{a_{1n}}{\sum_{t=1}^{n} a_{tn}} \\ \frac{a_{21}}{\sum_{n=1}^{n} a_{n1}} & \frac{a_{22}}{\sum_{n=1}^{n} a_{n2}} & \cdots & \frac{a_{2n}}{\sum_{t=1}^{n} a_{tn}} \\ \cdots & \cdots & \cdots & \cdots \\ \frac{a_{n1}}{\sum_{n=1}^{n} a_{n1}} & \frac{a_{n2}}{\sum_{n=1}^{n} a_{n2}} & \cdots & \frac{a_{nn}}{\sum_{t=1}^{n} a_{tn}} \end{bmatrix} = \begin{bmatrix} x_{11} & x_{12} & \cdots & x_{1n} \\ x_{21} & x_{22} & \cdots & x_{2n} \\ \cdots & \cdots & \cdots & \cdots \\ x_{n1} & x_{n2} & \cdots & x_{nn} \end{bmatrix} \tag{12}$$

The criteria weight vector, W, is calculated by averaging across the rows of X (Eq. (13)):

$$W = \frac{1}{n} \begin{bmatrix} \sum_{n=1}^{n} x_{1n} \\ \sum_{n=1}^{n} x_{2n} \\ \cdots \\ \sum_{t=1}^{n} x_{nt} \end{bmatrix} = \begin{bmatrix} w_1 \\ w_2 \\ \cdots \\ w_n \end{bmatrix} \tag{13}$$

$$\sum_{i=1}^{n} w_i = 1$$

The inconsistency of the pair-wise comparison matrix (CR) is then calculated with Eq. (14). In this equation, RI is the random consistency index, which is presented by Saaty (1988) in terms of the order of the pair-wise comparison matrix 2, and CI is the consistency index, which is calculated using Eq. (15). In this formula, λ_{max} is the maximum eigenvector of the pair-wise comparison matrix, estimated by Eq. (16).

$$CR = \frac{CI}{RI} \tag{14}$$

$$CI = \frac{\lambda_{max} - n}{n - 1} \tag{15}$$

$$A \times W = \lambda_{max} \times W \tag{16}$$

The inconsistency of subjective judgements of decision-makers is then assessed. If the consistency ratio is smaller than or equal to 0.1, the inconsistency is acceptable.

For the next step, the decision matrix using Eq. (17) is created:

$$D = \begin{array}{c} \\ A_1 \\ A_2 \\ \cdots \\ A_i \end{array} \begin{array}{c} \begin{array}{cccc} C_1 & C_2 & \cdots & C_j \end{array} \\ \begin{bmatrix} g_{11} & g_{12} & \cdots & g_{1j} \\ g_{21} & g_{22} & \cdots & g_{2j} \\ \cdots & \cdots & \cdots & \cdots \\ g_{i1} & g_{i2} & \cdots & g_{ij} \end{bmatrix} \end{array} \tag{17}$$

$$i = 1.2.\ldots.m$$

$$j = 1.2.\ldots.n$$

where, A_i denotes the alternatives i, C_j represents the jth criteria and g_{ij} is a crisp value that indicates the performance of each alternative with respect to each criterion. The decision matrix is then normalized using Eq. (18).

$$r_{ij} = \frac{g_{ij}}{\sqrt{\sum_{i=1}^{m} {g_{ij}}^2}} \tag{18}$$

The weighted normalized decision matrix is created using Eq. (19)

$$v_{ij} = w_j \cdot r_{ij} \tag{19}$$

The optimal positive and negative solutions are determined using Eqs. (20) and (21)

$$A^+ = \left\{ \left(\max v_{ij} | j \in J \right) or \left(\min v_{ij} | j \in J' \right) \right\} = \left\{ v_1^+ . v_2^+ . \ldots . v_n^+ \right\} \tag{20}$$

$$A^- = \left\{ \left(\min v_{ij} | j \in J \right) or \left(\max v_{ij} | j \in J' \right) \right\} = \left\{ v_1^- . v_2^- . \ldots . v_n^- \right\} \tag{21}$$

where J is the set of benefit or positive criteria, and J′ is the set of cost or negative criteria.

The distance D between the value inserted into the matrix using the n-dimensional Euclidean distance is calculated by Eqs. (22) and (23):

$$D_i^+ = \sqrt{\sum_{j=1}^{n} \left(v_{ij} - v_j^+ \right)^2} \tag{22}$$

$$D_i^- = \sqrt{\sum_{j=1}^{n} \left(v_{ij} - v_j^- \right)^2} \tag{23}$$

The relative closeness, RC, to the ideal solution is calculated using Eq. (24). The solutions are finally ranked based on descending order of RC.

$$RC = \frac{D_i^-}{D_i^+ + D_i^-} \tag{24}$$

7. Results and discussion

7.1. Base case results

The base case has an SM of 2 and a TES of 6 h. To compare the operation of the system in the chosen location, various other locations with solar potential have been chosen as well. Namely, Tucson of Arizona, USA; Almería of Andalusia, Spain; Xining of Qinghai, China; Chihuahua, Mexico; and Shiraz, Iran. A summary of the design point parameters is presented in Table 2. These are used similarly in all of the used locations.

The receiver thermal power required at the receiver outlet of the base case to meet the design thermal load is equal to 14.9

Table 2
Design point parameters of the base case.

Parameters	Values
Target receiver thermal power	14.9 MW_{th}
Field thermal output	15.1 MW_{th}
Actual SM	3.03
Total aperture reflective area	25 584 m^2
Solar field area	64 750 m^2
Actual number of loops	39
Loop optical efficiency	0.722
Total loop conversion efficiency	0.693
TES thermal capacity	44.6 MWh_{th}

MW_{th}. This is obtained by multiplying the SM with the heat sink power. The field thermal output is the delivered thermal energy of the SF under design conditions at the actual SM. The nominal thermal capacity of the storage system is equal to 44.6 MWh_{th}. A summary of the results of the system in the different locations is shown in Table 3.

Among the chosen locations, Shiraz and Tucson are found to result in the highest value of annual net energy of 34,775 and 34,038 MWh_{th}, respectively. Thus, these locations also have the highest amount of solar share, obtained by the ratio of annual net energy of the solar system over the annual required energy in the power block. Locations have also the lowest values of LCOH equal to 3.24 and 3.31 ¢/kWh, respectively. Xining results in the highest value of LCOH equal to 4.88, and the lowest amount of annual net energy (22,367 MWh), making Xining the place with the worst performance among the studied locations. For the initial case study in Kermanshah, the annual net energy is found to be equal to 28,841 MWh_{th}, and the LCOH equal to 3.85 ¢/kWh. To find out which type of solar system can increase the annual net energy considering the LCOH, a sensitivity analysis and optimization of the system is realized.

7.2. Sensitivity analyses and optimization

The hours of TES and the SM have a strong influence on the LCOH. The aim is to achieve the values for the SM and the hours of storage to minimize the energy cost, i.e., the LCOH. A lower LCOH results in a more profitable project with which more energy can be produced at a lower cost (Ezeanya et al., 2018). The required sensitivity analysis was realized in SAM and the obtained results are presented in Table 4. Fig. 5 also shows variation of the solar share with LCOH for various values of SM and TES hours.

The value of the SM controls the size of the solar collector, i.e., increasing the SM results in a SF with a larger reflective area that can provide more heat. The hours of storage specify the ability of the solar subsystem to store additional heat from the solar collector. Increasing the SM only makes sense when it is possible to use the excess heat at the same time. One option to use the excess heat is to store it and use at night-time, hence increasing the SM must, in most cases, be accompanied with an increase in the hours of storage. There exists an important relationship between SM and hours of storage. The case with 6 h of TES and an SM equal to 4 results in the highest value of LCOH (6.52 ¢/kWh). It is clear that the case with highest values of TES and SM (i.e., 24 and 4) has the highest amount of solar share. In this case, 50,346.4 MWh_{th} energy can be produced annually.

The LCOH and the solar share remain practically unchanged for different choices of hours of storage when the SM is below 2. This is because increasing the size of the SF by increasing the SM cannot provide more than six hours of heat duty to the plant (six hours of storage). As the SM gets higher than 2, the six hours of storage become inadequate, and it becomes beneficial both in terms of cost and solar share to have larger storage tanks. This is evident from the fact that the solar share of the six hours of storage curve stops rising for SM values above 2.2, whereas the solar share of curves associated with higher storage hours continues rising. The same argument can be used with the LCOH

Table 4
Results of the sensitivity analyses.

No. of runs	TES hours	Solar multiple, SM	Annual energy (MWh_{th})	Solar share (%)	LCOH (¢/kWh)
1	6	1	15 255.9	23.4	3.75
2	6	1.3	19 996.5	30.7	3.60
3	6	1.6	23 845.8	36.6	3.71
4	6	1.9	28 018.0	43	3.75
5	6	2.2	29 993.9	46	4.03
6	6	2.5	30 939.2	47.5	4.42
7	6	2.8	31 549.0	48.4	4.83
8	6	3.1	32 041.4	49.2	5.23
9	6	3.4	32 331.9	49.6	5.62
10	6	3.7	32 647.0	50.1	6.08
11	6	4	32 764.6	50.3	6.52
12	12	1	15 193.9	23.3	3.80
13	12	1.3	19 720.4	30.3	3.65
14	12	1.6	23 545.5	36.1	3.75
15	12	1.9	28 197.3	43.3	3.73
16	12	2.2	32 882.1	50.5	3.71
17	12	2.5	37 358.4	57.3	3.73
18	12	2.8	40 040.5	61.4	3.89
19	12	3.1	41 888.3	64.3	4.09
20	12	3.4	43 133.4	66.2	4.34
21	12	3.7	43 807.5	67.2	4.63
22	12	4	44 481.6	68.3	4.95
23	18	1	15 113.5	23.2	3.86
24	18	1.3	19 500.3	29.9	3.69
25	18	1.6	23 304.8	35.8	3.79
26	18	1.9	27 944.0	42.9	3.76
27	18	2.2	32 615.4	50	3.74
28	18	2.5	37 277.1	57.2	3.74
29	18	2.8	41 281.4	63.3	3.79
30	18	3.1	44 926.9	69.9	3.85
31	18	3.4	47 001.1	72.1	4.11
32	18	3.7	48 544.2	74.2	4.28
33	18	4	49 410.4	75.8	4.45
34	24	1	14 996.5	23	3.94
35	24	1.3	19 303.0	29.6	3.73
36	24	1.6	23 094.4	35.4	3.82
37	24	1.9	27 729.6	42.5	3.79
38	24	2.2	32 384.5	49.7	3.77
39	24	2.5	37 036.4	56.8	3.76
40	24	2.8	41 062.4	63	3.81
41	24	3.1	44 995.4	69	3.84
42	24	3.4	47 554.2	73	3.97
43	24	3.7	49 336.1	75.7	4.15
44	24	4	50 346.4	77.2	4.37

Table 3
Annual net energy and LCOH of the base case at different locations.

Parameters/Locations	Kermanshah	Shiraz	Tucson	Almeria	Xining	Chihuahua
Latitude	34.36	29.6	32.13	36.83	36.6	28.63
Longitude	47.43	52.53	−110.94	−2.46	101.7	−106.07
Collector tilt	34°	29.5°	32°	37°	36.5°	28.5°
Annual DNI (kW/m^2)	2157.8	2565.2	2687.9	2318.9	1690.4	2599.4
Solar share (%)	44.3	52.8	52.1	47.8	34.3	47.6
Annual net energy (MWh_{th})	28,841	34,775	34,038	31,057	22,367	31,062
Solar system LCOH (¢/kWh)	3.85	3.24	3.31	3.59	4.88	3.61

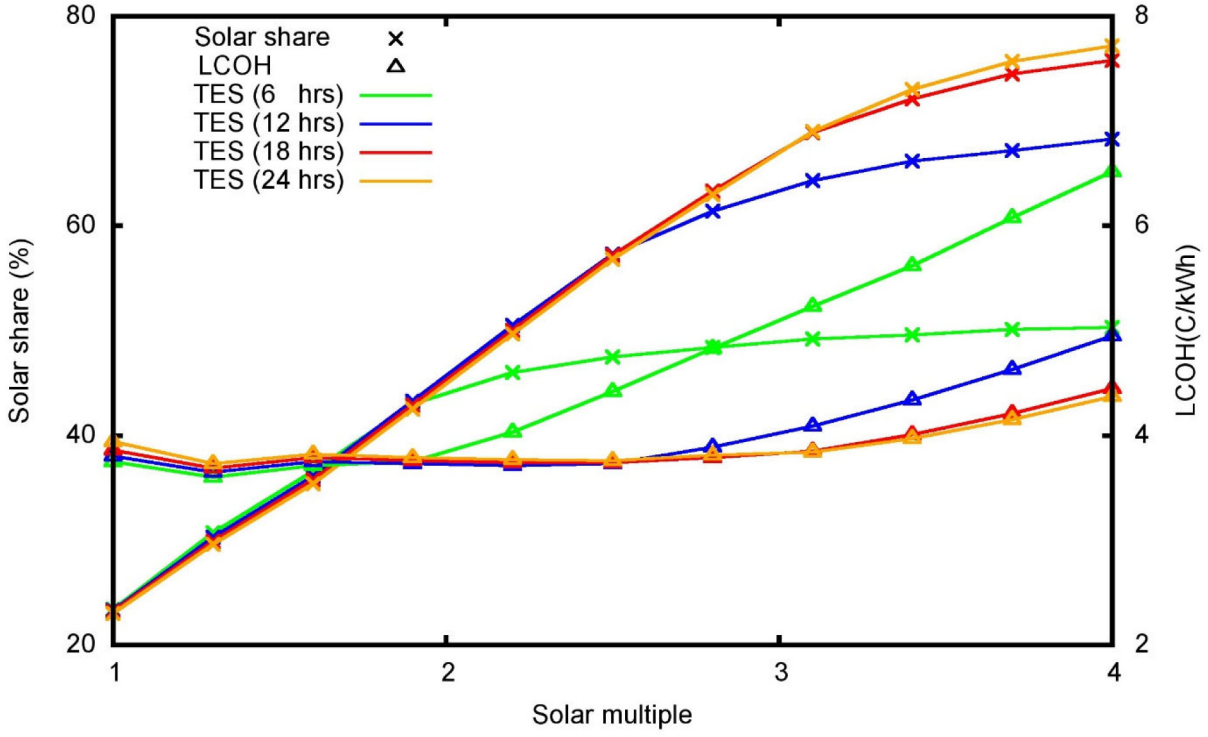

Fig. 5. Variation of the solar share and the LCOH with respect to various SM and TES hours.

curve. For six hours of storage, going beyond an SM of 2 does not yield any financial benefit in terms of fuel saving and it can be seen that the LCOH rises constantly because of the increasing cost of the SF.

The SM is also varied for different hours of TES with the goal to optimize the LCOH. The performance of the different scenarios with respect to LCOH and solar share variation at different values of the SM and hours of storage is presented in Fig. 6.

In this regard, four criteria with corresponding weights i.e., SM, (0.1); hours of TES, (0.1); solar share, (0.4); and LCOH, (0.4) have been considered. Weights for each criterion are obtained by the integrated AHP-TOPSIS and are then used to evaluate all alternative scenarios. Table 5 shows the RC to the ideal solution of all scenarios considered using the new pairwise comparison matrix. As expected, the 30th scenario is ranked first due to its relatively high solar share and acceptable LCOH. The relative closeness of this scenario to the ideal solution is equal to 0.817. After this scenario the scenarios 31th, 32th and 33th have the highest value of relative closeness, respectively.

The best performance is found when a point is located at the bottom right of the figure, where the highest solar share and the lowest LCOH can be achieved. The red points present the optimum cases, while for every blue point there is another blue or red point with a lower LCOH and a higher solar share. The point with the lowest solar share has also the lowest LCOH. The case with a solar share of 0.7 and a LCOH of 3.85 (¢/kWh) corresponding to an SM of 3.1 and 18-h of TES is selected. Ideally, the objective is to achieve solar shares about or greater than 70%, something that eliminates the points with considerably lower solar shares. In addition, a sharp increase of the LCOH after the selected point also eliminates the points with solar shares. The selected point achieves a relatively high solar share at a relatively low cost.

Table 5
The relative closeness of each scenario to the ideal solution.

No. of scenario	Value	Rank	No. of scenario	Value	Rank
1	0.406	41	23	0.375	43
2	0.457	34	24	0.425	39
3	0.492	30	25	0.459	33
4	0.547	24	26	0.524	27
5	0.562	22	27	0.599	20
6	0.552	23	28	0.680	17
7	0.529	26	29	0.749	12
8	0.504	29	30	0.817	1
9	0.477	31	31	0.815	2
10	0.450	35	32	0.815	3
11	0.428	38	33	0.807	4
12	0.390	42	34	0.361	44
13	0.440	37	35	0.412	40
14	0.475	32	36	0.444	36
15	0.541	25	37	0.506	28
16	0.619	19	38	0.578	21
17	0.699	16	39	0.653	18
18	0.746	13	40	0.715	15
19	0.772	9	41	0.768	10
20	0.775	8	42	0.790	6
21	0.754	11	43	0.792	5
22	0.725	14	44	0.781	7

7.3. Selected case analysis

A few control input and design parameters similar to ones presented in Section 4 are considered as the standard values for the PTC systems, whereas the rest are assumptions made based on other published research. The SF module computes the thermal output SF, and the thermal storage module computes the energy flow into the TES system and the thermal energy provided for to the reboiler. Like before, the case with an SM of 3.1 and 18-h of TES corresponding to a solar share of 0.7 and a LCOH of 3.85 (¢/kWh) is chosen. The SIPH system with a capacity of 7.44 MWh_{th} is designed based on PTC using as HTF Hitec XL and an 18-h indirect molten salt storage capacity at full load. Fig. 7(a) shows the heat sink thermal power following the required designed value, i.e., 7.44 MWh_{th}. It is clear that in the summer where the solar energy is sufficient, the system can operate independently based solely on solar. Some months,

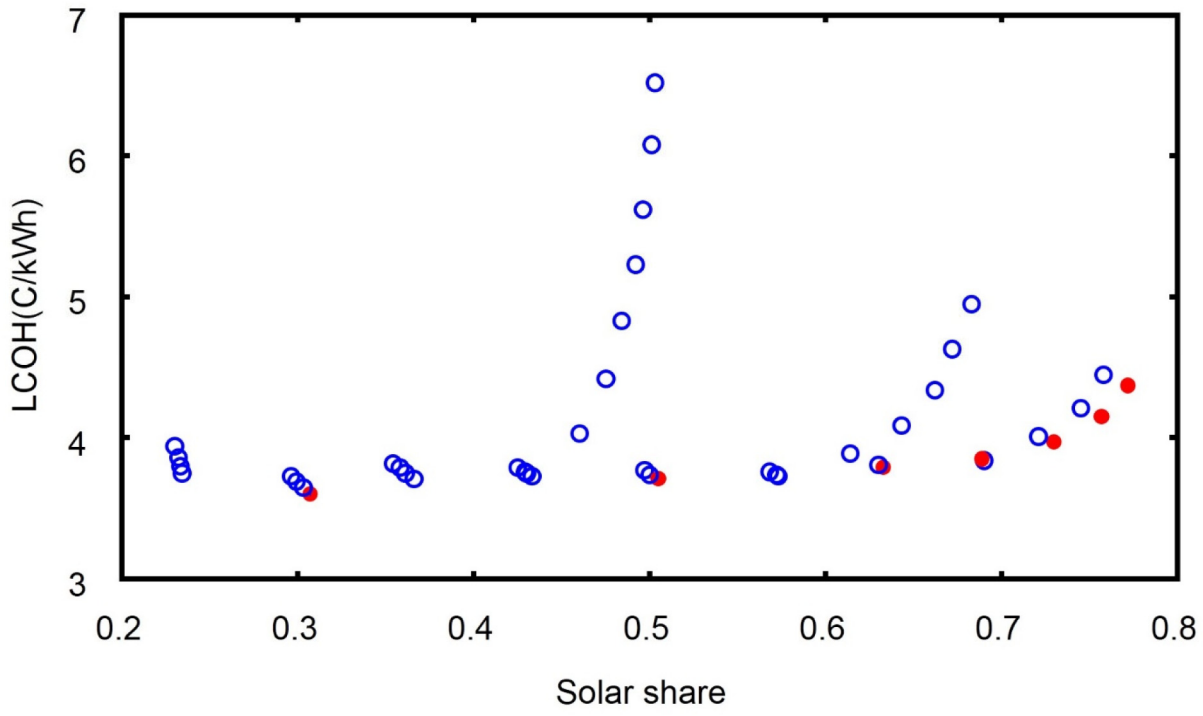

Fig. 6. Performance comparison of different cases by means of solar share and LCOH. (For interpretation of the references to colour in this figure legend, the reader is referred to the web version of this article.)

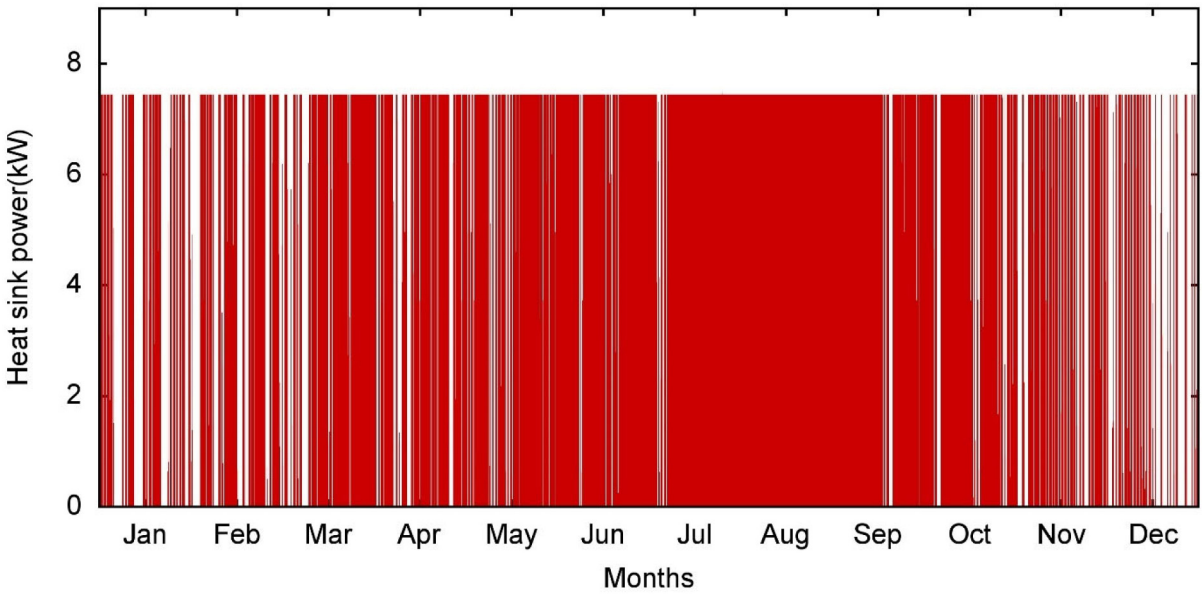

Fig. 7(a). The annually heat sink thermal power.

especially during the winter season, cloud formation prohibits, in many cases, the use of solar energy. The heat sink thermal power is presented here in Fig. 7(b) for two different months, i.e., January and July. The slope and quantity of the increment between 8 to 10 h is different in January and July, because the system in January is discharged totally at 8, while the system in July is almost working constantly using the saved energy in the storage system. The detailed results of the optimal case are presented in Table 6. Interesting conclusions can be obtained when comparing Table 6 with Table 2 that show the optimum system and the base case, respectively. Although both systems have the same value of LCOE (3.85 ¢/kWh), the annual net energy for the optimum case is 16,112 MWh_{th} higher than that of the base case system.

7.4. Transient analysis

The nominal thermal capacity of the storage system is obtained by multiplying the storage hours by the thermal power of the plant. Fig. 8 shows the charge state of 18 h of TES with maximum storage capacity about 135 MWh_{th}. When the charge state reaches this number, it means that the storage system can provide 18 h of storage, covering the entire night-time and possibly some cloudy periods during the day. The selected system

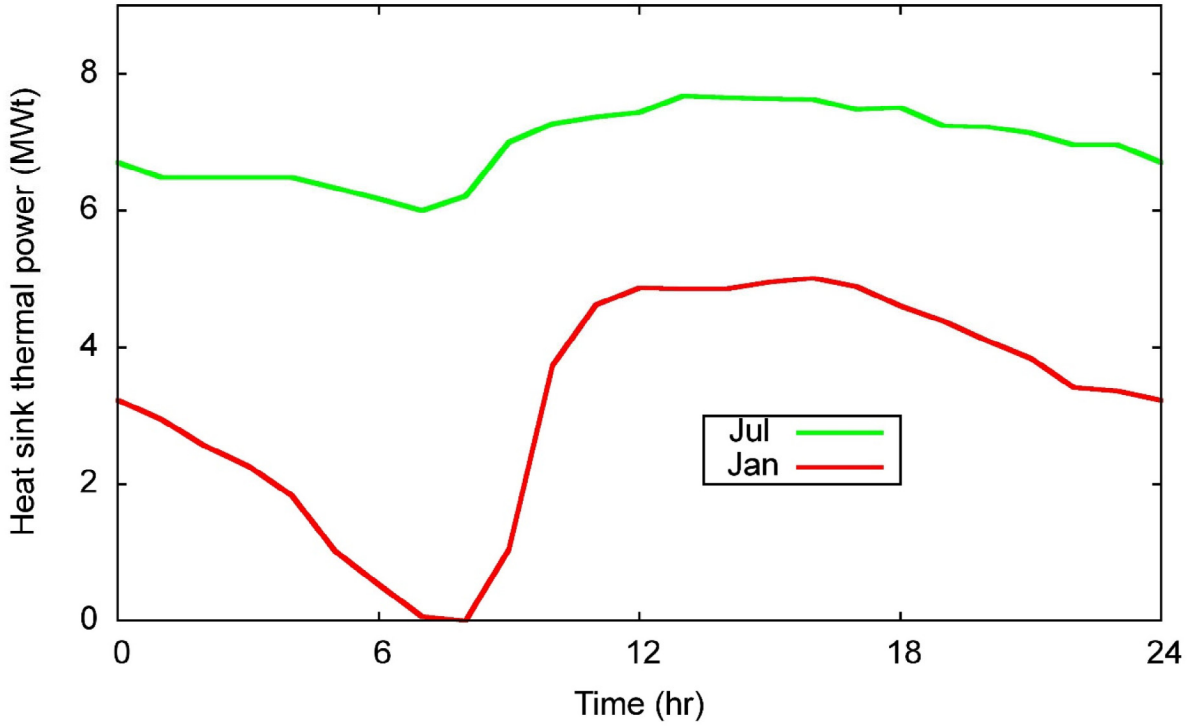

Fig. 7(b). The hourly heat-sink thermal power in January and July.

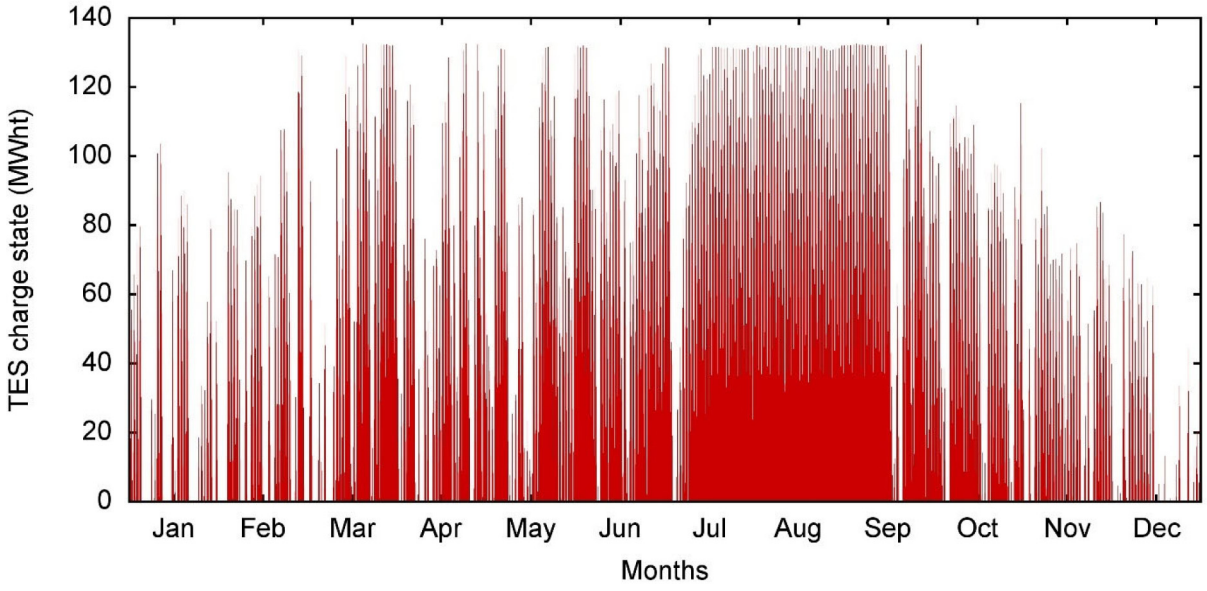

Fig. 8. TES charge state (MWh_{th}).

keeps the storage full almost throughout the entire summer. This means that the system can operate based solely on solar energy and without any backup for most of the summertime. But this is not the case during the winter season. In that case, the storage system never reaches its maximum capacity during January, February, November, and December. This reduces the annual solar share of the system to about 70%.

Fig. 9 shows the charge (a) and discharge (b) process of the TES on the summer solstice. To better understand how charging and discharging take place, the processes are presented for three different cases. The reference case with an SM of 3.1 and a TES of 18 h, the case with an SM of 4 and a TES of 6 h (case with the highest amount of LCOH), and the case with an SM of 4 and a TES of 24 h (case with the highest amount of solar share). The system charges between 7:30 to 15:30 and discharges during the rest of the day.

7.5. Share of solar and auxiliary energy

The amount of electricity that the power plant could have produced with the energy used in the CCS unit is obtaining with multiplying of annual total annual heat input (7.44*8760) with the efficiency of the power generation unit (30%), which is equal to 19.5 MW. To estimate which part of that energy would have come from the sun, we can multiply the 19.5 MW with the solar share (0.7) that results in 13.5 MW. The relative reduction in the

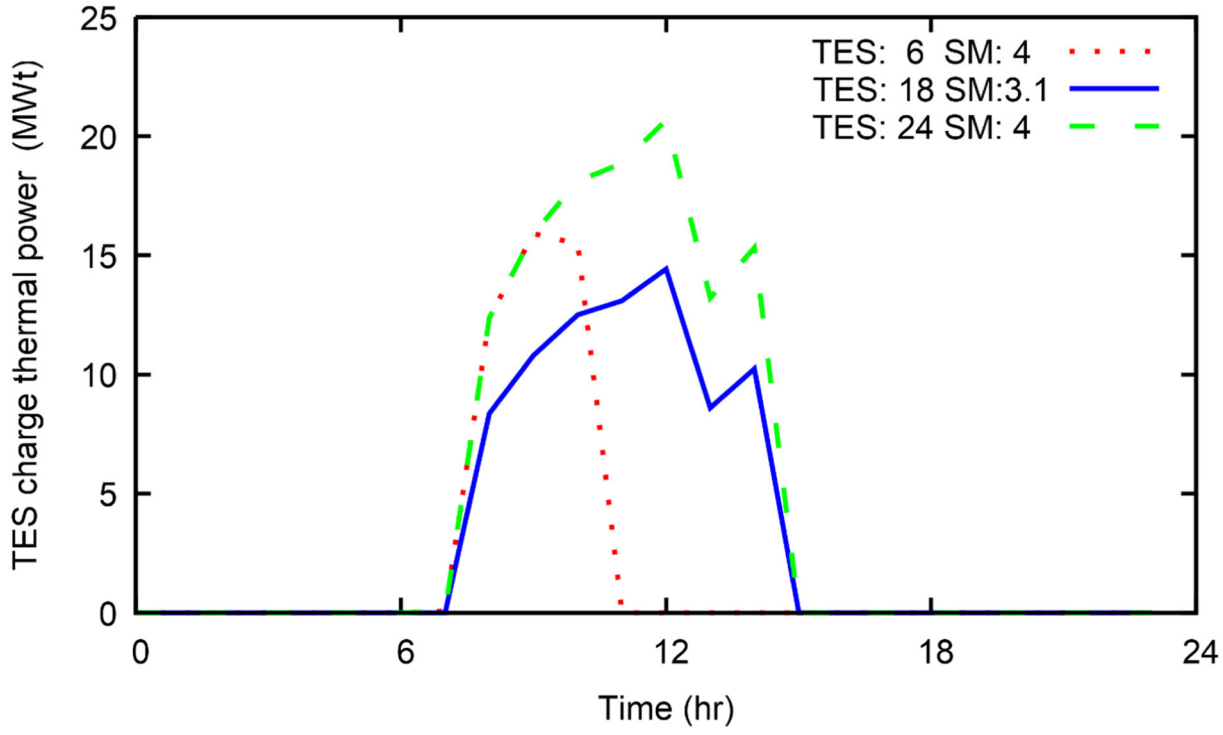

(a)

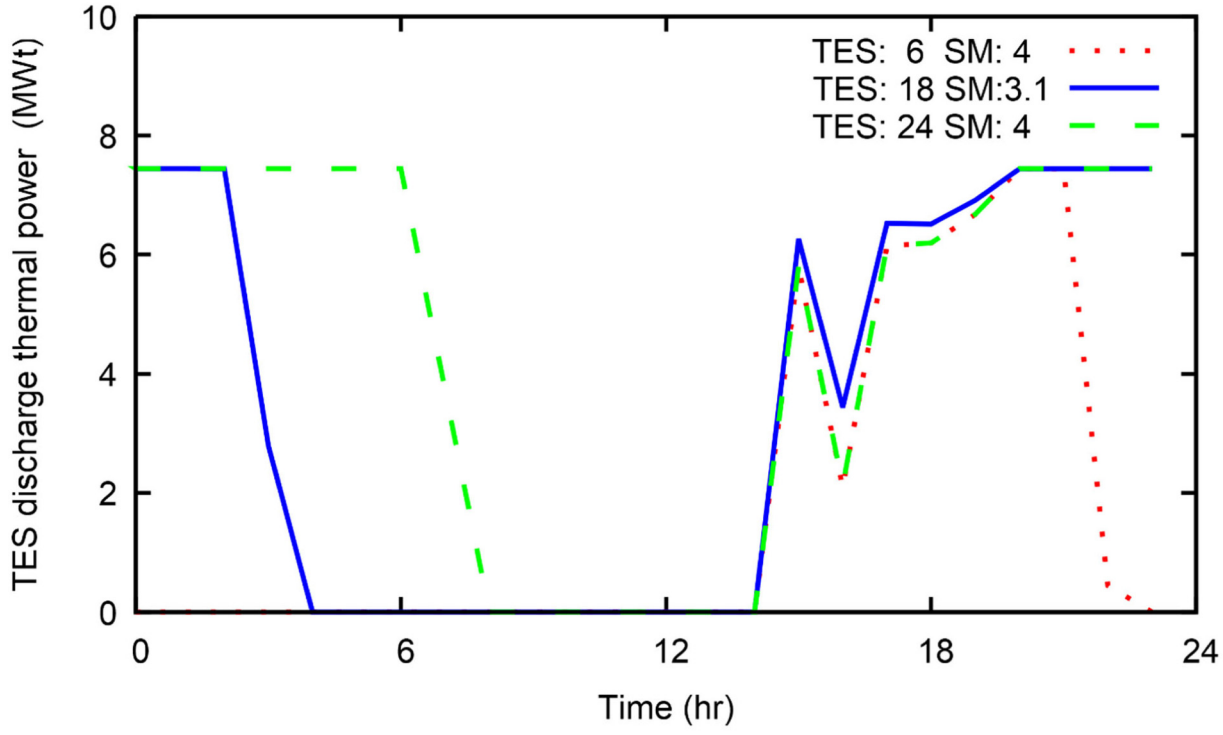

(b)

Fig. 9. TES charge (a) and discharge (b) on the summer solstice.

solar energy is thus equal to the solar share, found by dividing the 13.5 MW with the total amount of electricity produced if there were no CCU plant (19.5 MW).

To evaluate the amount of natural gas saved annually due to the incorporation of the solar system, a boiler with a 90% efficiency is assumed here. The flow rate of the steam used in the

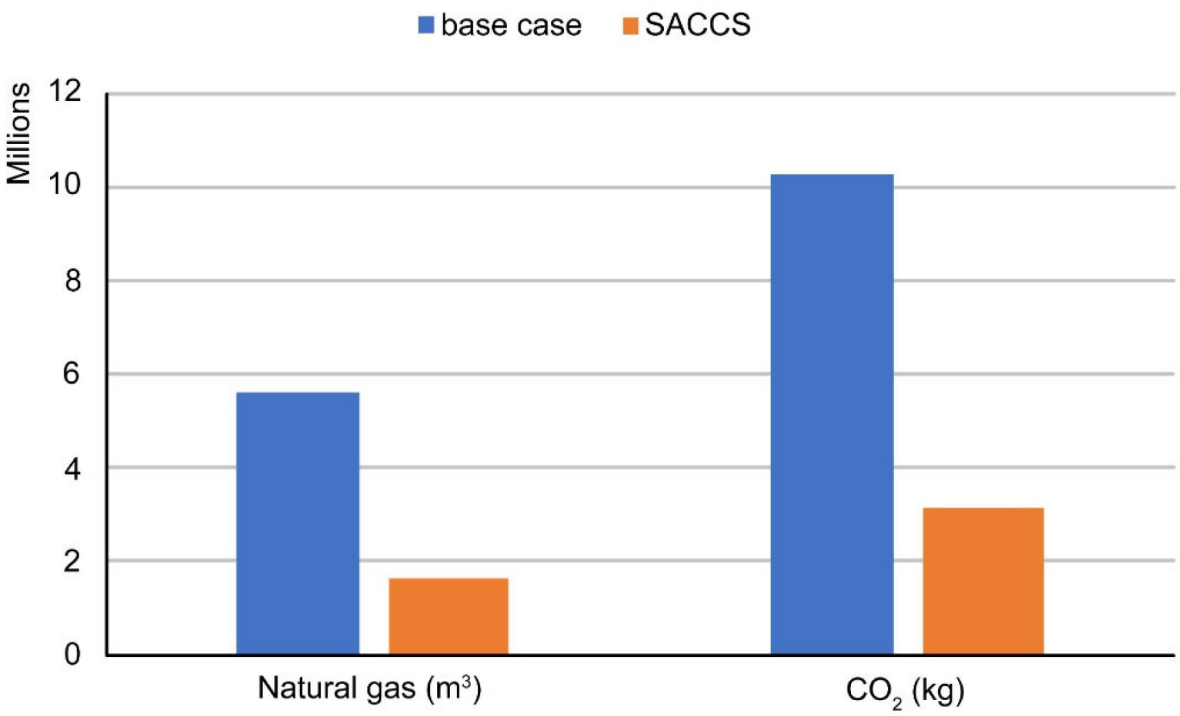

Fig. 10. Natural gas consumption and CO_2 emissions for the base case and the SACCS.

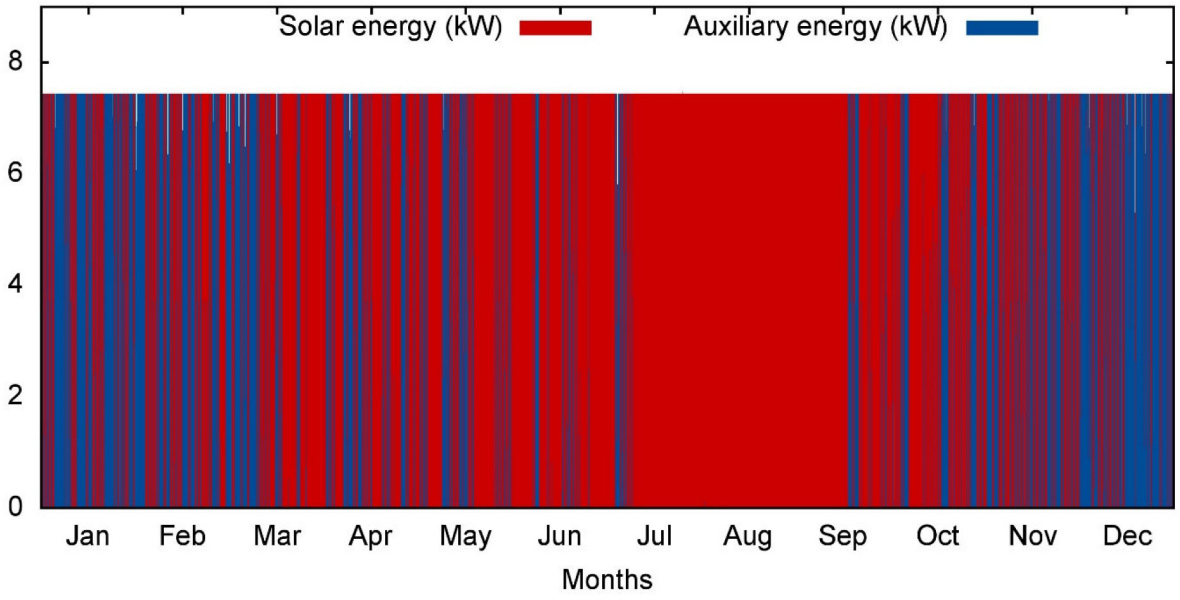

Fig. 11. Monthly share of solar energy versus auxiliary energy for stripper demand.

SR is equal to 11.5 tone/hr at 153 °C and 4.2 bar. The condensed steam has a temperature of 132 °C and a pressure of 3.8 bar. Considering the enthalpy of these points, almost 7440 kW heat is required to supply the thermal demand of the stripper. The amount of heat required in the steam generator, considering the boiler efficiency of 90%, is thus equal to 8266.6 kW. The volume flow rate of the required natural gas is then obtained by dividing the generated heat with the lower heating value of natural gas (47.1 MJ/m^3). It is found that approximately 5.5 million m^3 natural gas would be required to provide the demand of the stripper annually. Natural gas consists of CH_4 and minor quantities of ethane and heavier hydrocarbons and it burns as: $CH_4 + 2O_2 \rightarrow CO_2 + 2H_2O$. Natural gas volumes are measured at 15 °C and approximately 1 atm pressure, subsequently 1 m^3 results in 42.3 mol or 1.86 kg of CO_2. The system would thus release over 10 million kg CO_2 annually if it were fully supported by natural gas. With around 70 percent of the thermal required covered by the solar system, the natural gas consumption is reduced by approximately 3.8 million m^3. This leads to a similar reduction in the CO_2 emissions, that results in 7.1 kton of CO_2 avoided annually. Fig. 10 shows the amount of natural gas consumption and CO_2 emissions of the base case and the SACCS.

Fig. 11 shows the share of solar energy versus the auxiliary energy consumed annually in the integrated structure to provide the demand of the stripper. It is clear that from the middle of June and until September, the system can operate almost fully based

Table 6
Selected system results of the optimum case.

Parameters	Value
Target receiver thermal power	23.06 MW_{th}
Field thermal output	23.2 MW_{th}
Actual SM	3.12
Total aperture reflective area	39,360 m^2
Solar field area	97,124 m^2
Actual number of loops	60
Loop optical efficiency	0.722
Total loop conversion efficiency	0.693
TES thermal capacity	133.9 MWh_{th}
Annual net energy	44,926.9 MWh_{th}

on the solar system. Fig. 12 shows the share of solar energy versus the auxiliary energy at different hours of June 21. It is seen that the system required auxiliary energy between 3–6 am to operate continuously.

8. Conclusion

This paper presented the techno-economic analysis of a solar-assisted post-combustion carbon capture system. A solar industrial process heat unit was modelled using parabolic trough collectors to provide the required regeneration heat of the solvent in the carbon capture process. The thermal energy required for the regeneration of the solvent was calculated in dynamic simulations supported by hourly solar irradiation data obtained from the European Commission's Photovoltaic Geographical Information System (PVGIS). Sensitivity analyses of critical variables were then realized with the goal to optimize the structure and minimize the levelized cost of the generated heat. The case with a solar multiple of 3.1 and a thermal energy storage of 18-h was selected with a solar share of 0.7 and a levelized cost of heat of 3.85 ¢/kWh. Although the optimum case had a similar cost to the base case, the first resulted in a higher annual generation of net energy (44,927 MWh_{th} versus 28,815 MWh_{th}). The transient analysis realized showed that the system used the storage unit during the summer almost continuously and generated the required heat for the solvent regeneration. With 18 h of storage, it also reached about 135 MW, covering a large part of the night-time operation and some cloudy periods during the day. When the sunlight is insufficient during the winter, however, the solar system cannot provide the required thermal energy for the regenerator. For example, the storage system never reaches its maximum capacity in January, February, November, and December. This reduces the annual solar share of the plant to about 70%. Considering that 70% of the thermal energy required is supplied by the solar system, the annual natural gas consumption and CO_2 emissions are decreased by approximately 3.8 million m^3 and 7.1 kton, respectively.

Nomenclature

AEP	Annual Energy Production
AHP	Analytic Hierarchy Process
CCS	Carbon Capture System
CCU	Carbon Capture and Utilization
CPC	Compound Parabolic Collector
CRF	Capital Recovery Factor
CFF	Construction Financing Factor
CINT	Nominal construction financing interest rate
DSA	Direct Solar Assisted
ETC	Evacuated Tube Collector
FCR	Fixed Charge Rate
FOC	Fixed annual Operating Cost
FPC	Flat Plate Collector
HTF	Heat Transfer Fluid
IPH	Industrial Process Heat
ISA	Indirect Solar Assisted
IRR	Nominal return on investment
LFC	Linear Fresnel Collector
NINT	Nominal-debt interest rate
NREL	National Renewable Energy Laboratory
PCC	Post-combustion Carbon Capture
PFF	Project Financing Factor
PTC	Parabolic Trough Collector
PVDEP	Present Value of Depreciation
RROE	Real Return on Investment
RINT	Real-debt Interest rate
SAM	System Advisor Model
SF	Solar Field
SIPH	Solar Industrial Process Heat
STC	Solar Thermal Collector
TCC	Total Capital Cost ($)
TOPSIS	Technique for Order Preference by Similarity to Ideal Solution
RC	Relative Closeness
SPCC	Solar-assisted Post-combustion Carbon Capture
SACCS	Solar-assisted Carbon Capture System
SM	Solar multiple
STE	Solar Thermal Energy
SR	Solvent Regeneration
TES	Thermal Energy Storage
VOC	Variable Operating Cost ($/kWh)
WACC	Weighted Average Cost of Capital

CRediT authorship contribution statement

Reza Shirmohammadi: Conceptualization, Methodology, Software, Formal analysis, Visualization, Writing - original draft, Review & editing. **Alireza Aslani:** Project administration, Supervision, Resources, Review & editing. **Roghayeh Ghasempour:** Project administration, Supervision, Resources, Review & editing.. **Luis M. Romeo:** Supervision, Conceptualization, Review & editing. **Fontina Petrakopoulou:** Supervision, Writing – review & editing.

Declaration of competing interest

The authors declare that they have no known competing financial interests or personal relationships that could have appeared to influence the work reported in this paper.

Acknowledgement

The corresponding authors would like to acknowledge the University of Tehran and the Iran's National Elites Foundation for providing support at this work. The authors would also like to thank Paul Gilman from SAM support at the National Renewable Energy Laboratory. Last but not least, technical supports of the Kermanshah Petrochemical Industries Co. and the Shahrekord Carbon Dioxide Co. are gratefully acknowledged.

Fontina Petrakopoulou would like to thank the Spanish Ministry of Science, Innovation and Universities and the Universidad Carlos III de Madrid (Ramón y Cajal Programme, RYC-2016-20971).

Appendix

The detailed results related to solar field parameters, collector, receiver, and storage system are presented in the following table. Heat sink power in conjunction with the target SM determines the receiver design conditions (see Table A.1).

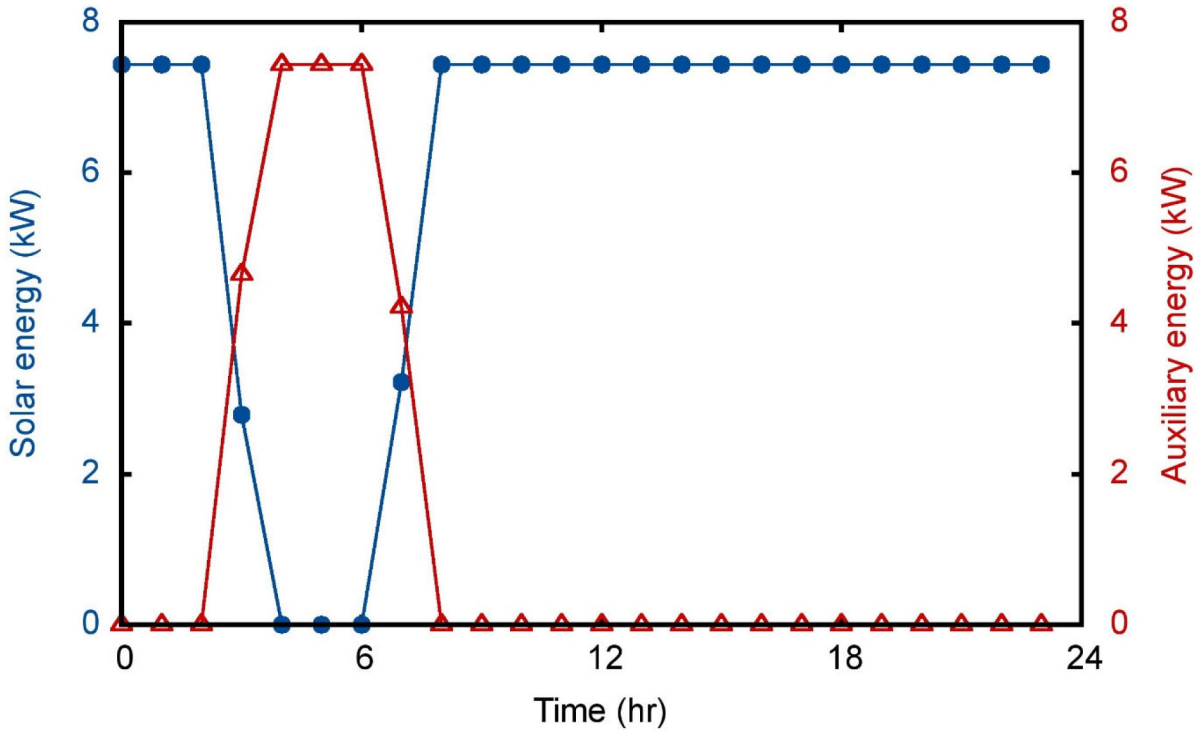

Fig. 12. Share of solar energy versus auxiliary energy consumed in the process at different hours of a specific day (21 June).

Table A.1
Detailed results of the developed solar system.

Solar field			
Loop inlet HTF temperature	150 °C	Pumping power for HTF through heat sink	0.55 kW/kg/s
Loop inlet HTF temperature	170 °C	Single loop Aperture	656 m^2
Row Spacing	15 m	Min single loop flow rate	1 kg/s
HTF Pump efficiency	0.85	Max single Loop flow rate	15 kg/s
Collector tilt	34°	Min field flow velocity	0.1 m/s
Collector azimuth	0°	Max field flow velocity	1.6 m/s
Stow Angle	170°	Header design min flow velocity	1 m/s
Deploy Angle	10°	Header design max flow velocity	3 m/s
Field HTF Fluid	Hitec XL	Water usage per wash for mirror	0.7 L/m^2
Freeze protection temp.	120	Washes per year	12
Field HTF min operating temp.	238 °C	Assemblies No. of SCA/HCE per loop	8
Field HTF max operating temp.	593 °C	SF area	24 acres
Filed loop piping thermal inertia	4.5 Wht/K-m	Total land area	27 acres
Collector			
Configuration of collector	SFST	Piping distance between assemblies	1 m
Reflective Aperture Area	656 m^2	Length of the single Module	14.375 m
Aperture width, total Structure	6 m	Tracking error	0.988
Length of the collector Assembly	115 m	Geometry effect	0.952
Number of modules per assembly	8	Mirror reflectance	0.93
Average Surface to focus path length	2.15 m	Dirt on mirror	0.97
IAM at summer solstice	0.93	General optical error	1
Receiver			
Receiver name	Siemens UVAC	Internal surface roughness	4.5e−05
Inner diameter of absorber tube	0.066 m	Inner diameter of glass envelope	0.109 m
Outer diameter of absorber tube	0.07 m	Outer diameter of glass envelope	0.115 m
Absorptance of absorber	0.96	Absorptance of envelope	0.02
Emittance of absorber	0.65	Emittance of envelope	0.89
Total heat weighted losses	192 W/m	Transmittance of envelope	0.965
Thermal storage			
TES thermal capacity	133.9 MWt-hr	Volume of storage tank	7934 m^3
Wetted loss coefficient	0.3 Wt/m^2-K	Estimated heat loss	0.22 MWt

References

Blair, N., Dobos, A.P., Freeman, J., Neises, T., Wagner, M., Ferguson, T., …, Janzou, S., 2014. System advisor model, sam 2014.1. 14: General description. Retrieved from.

Brodrick, P.G., Kang, C.A., Brandt, A.R., Durlofsky, L.J., 2015. Optimization of carbon-capture-enabled coal-gas-solar power generation. Energy 79, 149–162.

Carapellucci, R., Giordano, L., Vaccarelli, M., 2015a. Analysis of CO2 post-combustion capture in coal-fired power plants integrated with renewable energies. Energy Procedia 82, 350–357.

Carapellucci, R., Giordano, L., Vaccarelli, M., 2015b. Co2 post-combustion capture in coal-fired power plants integrated with solar systems. J. Phys. Conf. Ser. 655 (1), 012010.

Dubois, L., Thomas, D., 2018. Comparison of various configurations of the absorption-regeneration process using different solvents for the post-combustion CO2 capture applied to cement plant flue gases. Int. J. Greenhouse Gas Control 69, 20–35. http://dx.doi.org/10.1016/j.ijggc.2017.12.004.

Ezeanya, E.K., Massiha, G.H., Simon, W.E., Raush, J.R., Chambers, T.L., 2018. System advisor model (SAM) simulation modelling of a concentrating solar thermal power plant with comparison to actual performance data. Cogent Eng. 5 (1), 1524051.

Flores-Granobles, M., Saeys, M., 2020. Minimizing CO 2 emissions with renewable energy: a comparative study of emerging technologies in the steel industry. Energy Environ. Sci. 13 (7), 1923–1932.

Ghoniem, A.F., 2011. Needs, resources and climate change: clean and efficient conversion technologies. Prog. Energy Combust. Sci. 37 (1), 15–51.

Gutierrez, R.E., Haro, P., Gomez-Barea, A., 2021. Techno-economic and operational assessment of concentrated solar power plants with a dual supporting system. Appl. Energy 302, 117600.

Iribarren, D., Petrakopoulou, F., Dufour, J., 2013. Environmental and thermodynamic evaluation of CO2 capture, transport and storage with and without enhanced resource recovery. Energy 50, 477–485. http://dx.doi.org/10.1016/j.energy.2012.12.021.

Khalilpour, R., Milani, D., Qadir, A., Chiesa, M., Abbas, A., 2017. A novel process for direct solvent regeneration via solar thermal energy for carbon capture. Renew. Energy 104, 60–75.

Li, H., Yan, J., Campana, P.E., 2012. Feasibility of integrating solar energy into a power plant with amine-based chemical absorption for CO2 capture. Int. J. Greenhouse Gas Control 9, 272–280.

Lopes, F.M., Conceição, R., Fasquelle, T., Silva, H.G., Salgado, R., Canhoto, P., Collares-Pereira, M., 2020. Predicted direct solar radiation (ECMWF) for optimized operational strategies of linear focus parabolic-trough systems. Renew. Energy 151, 378–391.

Mokheimer, E.M.A., Shakeel, M.R., Sanusi, Y.S., Mahmoud, M., 2020. Thermo-economic comparative analysis of solar-assisted and carbon capture integrated conventional cogeneration plant of power and process steam. Int. J. Energy Res. 44 (11), 8455–8479. http://dx.doi.org/10.1002/er.5532.

Mokhtar, M., Ali, M.T., Khalilpour, R., Abbas, A., Shah, N., Al Hajaj, A., ., Sgouridis, S., 2012. Solar-assisted post-combustion carbon capture feasibility study. Appl. Energy 92, 668–676.

Parvareh, F., Milani, D., Sharma, M., Chiesa, M., Abbas, A., 2015. Solar repowering of PCC-retrofitted power plants; solar thermal plant dynamic modelling and control strategies. Sol. Energy 119, 507–530.

Parvareh, F., Sharma, M., Qadir, A., Milani, D., Khalilpour, R., Chiesa, M., Abbas, A., 2014. Integration of solar energy in coal-fired power plants retrofitted with carbon capture: a review. Renew. Sustain. Energy Rev. 38, 1029–1044.

Petrakopoulou, F., Tsatsaronis, G., 2014. Can carbon dioxide capture and storage from power plants reduce the environmental impact of electricity generation? Energy Fuels 28 (8), 5327–5338. http://dx.doi.org/10.1021/ef500925h.

Petrakopoulou, F., Tsatsaronis, G., Boyano, A., Morosuk, T., 2012. Post-Combustion CO2 Capture with Monoethanolamine in a Combined-Cycle Power Plant: Exergetic, Economic and Environmental Assessment *Greenhouse Gases–Emission, Measurement and Management*. InTech–Open Access Company.

Pvgis, E., 2018. Photovoltaic geographical information system.

Qadir, A., Carter, L., Wood, T., Abbas, A., 2015a. Economic and policy evaluation of SPCC (solar-assisted post-combustion carbon capture) in Australia. Energy 93, 294–308.

Qadir, A., Mokhtar, M., Khalilpour, R., Milani, D., Vassallo, A., Chiesa, M., Abbas, A., 2013. Potential for solar-assisted post-combustion carbon capture in Australia. Appl. Energy 111, 175–185.

Qadir, A., Sharma, M., Parvareh, F., Khalilpour, R., Abbas, A., 2015b. Flexible dynamic operation of solar-integrated power plant with solvent based post-combustion carbon capture (PCC) process. Energy Convers. Manage. 97, 7–19.

Saaty, T.L., 1988. What is the analytic hierarchy process? In: Mathematical Models for Decision Support. Springer, pp. 109–121.

Saghafifar, M., Gabra, S., 2020. A critical overview of solar assisted carbon capture systems: Is solar always the solution? Int. J. Greenhouse Gas Control 92, 102852. http://dx.doi.org/10.1016/j.ijggc.2019.102852.

Salkuyeh, Y.K., Mofarahi, M., 2012. Comparison of MEA and DGA performance for CO2 capture under different operational conditions. Int. J. Energy Res. 36 (2), 259–268. http://dx.doi.org/10.1002/er.1812.

Schoeneberger, C.A., McMillan, C.A., Kurup, P., Akar, S., Margolis, R., Masanet, E., 2020. Solar for industrial process heat: A review of technologies, analysis approaches, and potential applications in the United States. Energy 206, 118083. http://dx.doi.org/10.1016/j.energy.2020.118083.

Shirmohammadi, R., Aslani, A., Ghasempour, R., 2020a. Challenges of carbon capture technologies deployment in developing countries. Sustain. Energy Technol. Assess. 42, 100837. http://dx.doi.org/10.1016/j.seta.2020.100837.

Shirmohammadi, R., Aslani, A., Ghasempour, R., Romeo, L.M., 2020b. CO2 utilization via integration of an industrial post-combustion capture process with a urea plant: Process modelling and sensitivity analysis. Processes 8 (9), 1144.

Shirmohammadi, R., Aslani, A., Ghasempour, R., Romeo, L.M., Petrakopoulou, F., 2021. Process design and thermoeconomic evaluation of a CO2 liquefaction process driven by waste exhaust heat recovery for an industrial CO2 capture and utilization plant. J. Thermal Anal. Calorimetry http://dx.doi.org/10.1007/s10973-021-10833-z.

Shirmohammadi, R., Soltanieh, M., Romeo, L.M., 2018. Thermoeconomic analysis and optimization of post-combustion CO2 recovery unit utilizing absorption refrigeration system for a natural-gas-fired power plant. Environ. Progr. Sustain. Energy 37 (3), 1075–1084. http://dx.doi.org/10.1002/ep.12866.

Siddiqui, O., Ishaq, H., Chehade, G., Dincer, I., 2020. Performance investigation of a new renewable energy-based carbon dioxide capturing system with aqueous ammonia. Int. J. Energy Res. 44 (3), 2252–2263. http://dx.doi.org/10.1002/er.5087.

Wang, J., Liu, L., Zeng, X., Li, K., 2021a. Solar-assisted CO2 capture with amine and ammonia-based chemical absorption: A comparative study. Therm. Sci. 25 (1 Part B), 717–732.

Wang, J., Sun, T., Zeng, X., Fu, J., Zhao, J., Deng, S., Li, K., 2021b. Feasibility of solar-assisted CO2 capture power plant with flexible operation: A case study in China. Appl. Therm. Eng. 182, 116096. http://dx.doi.org/10.1016/j.applthermaleng.2020.116096.

Wang, F., Zhao, J., Li, H., Deng, S., Yan, J., 2017a. Preliminary experimental study of post-combustion carbon capture integrated with solar thermal collectors. Appl. Energy 185, 1471–1480.

Wang, F., Zhao, J., Li, H., Li, H., Zhao, L., Yan, J., 2015. Experimental study of solar assisted post-combustion carbon capture. Energy Procedia 75, 2246–2252.

Wang, J., Zhao, J., Wang, Y., Deng, S., Sun, T., Li, K., 2017b. Application potential of solar-assisted post-combustion carbon capture and storage (CCS) in China: A life cycle approach. J. Cleaner Prod. 154, 541–552.

Wibberley, L., 2010. Co2 Capture using Solar Thermal Energy. US Patents.

Zhai, R., Qi, J., Zhu, Y., Zhao, M., Yang, Y., 2017. Novel system integrations of 1000 MW coal-fired power plant retrofitted with solar energy and CO2 capture system. Appl. Therm. Eng. 125, 1133–1145.

Zhao, Y., Hong, H., Zhang, X., Jin, H., 2012. Integrating mid-temperature solar heat and post-combustion CO2-capture in a coal-fired power plant. Sol. Energy 86 (11), 3196–3204.

Zhao, L., Zhao, R., Deng, S., Tan, Y., Liu, Y., 2014. Integrating solar organic rankine cycle into a coal-fired power plant with amine-based chemical absorption for CO2 capture. Int. J. Greenhouse Gas Control 31, 77–86.